Catalysis Science & Technology

ROYAL SOCIETY OF CHEMISTRY

PAPER

View Article Online
View Journal





Cite this: DOI: 10.1039/c9cy01886g

# Heteroatom substituted zeolite FAU with ultralow Al contents for liquid-phase oxidation catalysis†

Daniel T. Bregante, [a] Jun Zhi Tan,[a] Andre Sutrisno[b] and David W. Flaherty*[a]

Received 18th September 2019,
Accepted 3rd November 2019

DOI: 10.1039/c9cy01886g

rsc.li/catalysis

Heteroatom framework-substituted zeolites are important materials that enable shape- and size-selective catalysis. The efficacy of these materials for desired catalytic reactions depends critically on dispersive interactions between the microporous void of the zeolite and the reactant molecules stabilized within it. Here, we develop a post-synthetic method to synthesize base and transition metal-substituted (Ti, Nb, Ta, and Sn) FAU with ultralow Al contents (Si : Al > 900), which is confirmed using X-ray diffraction, elemental analysis, and $N_2$ volumetric adsorption and $^{29}$Si MAS-NMR, DRUV-vis, and IR spectroscopic characterization. Turnover rates for styrene ($C_8H_8$) epoxidation within Ti-FAU are 2- and 7-fold greater than in analogous Ti-BEA and Ti–$SiO_2$, respectively; yet, turnover rates of $H_2O_2$ decomposition are similar for all three materials. Consequently, Ti-FAU gives greater rates and selectivities for this reaction than common Ti-bearing silicates. The mechanism for epoxidation remains constant for all Ti-silicates examined (*i.e.*, Ti-FAU, Ti-BEA, and Ti–$SiO_2$). Therefore, the improved performance of Ti-FAU reflects differences in activation free energies for epoxidation that show an enthalpic preference in Ti-FAU relative to Ti–$SiO_2$ and an entropic gain relative to Ti-BEA. These results demonstrate the synthesis of M-FAU with ultralow Al contents are useful for catalytic reactions involving bulky reactants that can not occur in smaller pore zeotype materials (Ti-MFI), that exhibit deactivation due to changes in Ti-atom coordination (*e.g.*, Ti–$SiO_2$), and that are prone to losses catalyzed by residual Brønsted acid sites (*e.g.*, epoxidations, oxidations, and isomerization reactions).

## Introduction

Decades of research[1–8] devoted to zeolite and zeotype catalysts have focused on understanding how the unique pore structure of these materials enables size- and shape-selective catalysis. The rates and selectivities toward specific, desired catalytic transformations depends critically on the dispersive interactions between the micropores of the zeolite catalyst and the reactants contained within these spaces.[6,9,10] These interactions provide a basis to modify rates and selectivities by stabilizing surface intermediates and transition states along reaction coordinates.

Zeolite catalysts that contain framework-substituted Lewis acidic heteroatoms (*e.g.*, Ti, Sn, Nb, Ta) catalyse stereoselective mono- and di-saccharide isomerization,[11,12] aldol condensation,[13–15] alcohol dehydration,[16,17] Baeyer–Villiger oxidation,[18–20] and alkene epoxidation reactions.[18,21–26] For example, the discovery that Sn-substituted zeolite *BEA (Sn-BEA) activates ketones for Baeyer–Villiger oxidation[25] with hydrogen peroxide ($H_2O_2$) catalysed a renaissance of work with Sn-BEA for use in other reactions (*e.g.*, glucose isomerization,[11,27] ethanol dehydration[16,17]). Titanium-substituted silicalite-1 (TS-1) was developed in the 1980's and has found industrial application as a catalyst for propylene epoxidation with $H_2O_2$,[26] which inspired the development of subsequent design principles for epoxidation reactions.[3,4,10,22–24,28–31] The presence of Brønsted acid sites (*e.g.*, those formed at framework Al or B atoms) catalyse secondary reactions that are detrimental to the desired chemistry, even when Al atoms remain in trace quantities (Si : Al = 10–150).[32–35] In the context of alkene epoxidation, the desired epoxides formed by primary reaction pathways readily undergo undesirable ring opening hydrolysis over Brønsted acids,[36] which decreases yields. Therefore, researchers invested significant effort into developing synthetic methods that avoid forming these deleterious sites through direct hydrothermal synthesis[11,27,28] or through the post-synthetic removal of adventitious Al atoms.[37–39]

The zeolite faujasite (FAU) is an important structure used in 95% of the catalyst market (by mass),[40] due to its widespread use in fluid catalytic cracking units. The

[a] *Department of Chemical and Biomolecular Engineering, University of Illinois at Urbana-Champaign, Urbana, IL 61801, USA. E-mail: dwflhrty@illinois.edu*
[b] *NMR/EPR Laboratory, School of Chemical Sciences, University of Illinois at Urbana-Champaign, Urbana, IL 61801, USA*

† Electronic supplementary information (ESI) available. See DOI: 10.1039/c9cy01886g

synthesis of Al-free metal-substituted FAU (M-FAU) materials have not been reported, despite the widespread use of this framework in the oil and gas industries. Current methods for the synthesis of M-FAU either rely on the post-synthetic modification of Al-FAU[20,41–43] or direct hydrothermal synthesis in the presence of $AlNaO_2$.[44] For example, Trejda *et al.* synthesized Nb- and Ta-substituted FAU hydrothermally in the presence of sodium aluminate (needed to crystalize the structure) yet, this approach produced in M-Al-FAU materials with a Si : Al ratio equal to 2.3.[44] Methods for the post-synthetic modification of Al-FAU rely on steaming at high temperatures[41] or acid treatments[20,42] to partially remove Al from framework positions and create vacant silanol nest ($(SiOH)_4$) defects that can be substituted with the desired metal atoms. In all previous reports, a significant amount of Al (Si : Al ratios = 19–150) remains,[20,41–43,45] which is detrimental for a number of relevant reactions. Consequently, the advent of synthetic methods to produce Al-free M-FAU would be impactful for numerous industrially practiced catalytic reactions including alkene epoxidation and biomass upgrading.

Here, we show that sequential treatments of Al-FAU in concentrated $HNO_3$ removes nearly all of the Al within these materials and increase Si : Al ratios from 15 to values greater than 900. The incorporation of base and early-transition metals into the FAU framework preserves the crystallinity of these materials and is confirmed using a combination of techniques including X-ray diffraction, $N_2$ volumetric adsorption, diffuse-reflectance UV-vis spectroscopy, $^{29}Si$ nuclear magnetic resonance spectroscopy, and infrared spectroscopy. Infrared spectra of pyridine adsorbed within M-FAU synthesize by these methods show the presence of Lewis acid sites and undetectable numbers of Brønsted acid sites (within the sensitivity of the method).

Comparisons of the rates, selectivities, and yields for styrene ($C_8H_8$) epoxidation with $H_2O_2$ over Ti-FAU to that in other Ti-silicates demonstrates advantages of locating Ti active sites within the supercages of the FAU structure. Turnover rates for styrene epoxidation over Ti-FAU are 2- and 7-fold greater than those in Al-free Ti-BEA (0.65 nm pore diameter) and Ti–$SiO_2$ (5.4 nm pore diameter), respectively. Rates of $H_2O_2$ decomposition (2.7 ± 0.9 (mmol $H_2O_2$)(mol Ti × s)$^{-1}$) remain constant for all structures, and therefore, do not depend on the characteristic dimensions of these Ti-silicate catalysts. Consequently, Ti-FAU gives greater selectivities and greater turnover rates for styrene epoxidation than Ti-BEA and Ti–$SiO_2$. Mechanistic interpretation of epoxidation rates measured as a function of reactant concentrations show that all Ti-silicates irreversibly activate $H_2O_2$ to form Ti–OOH intermediates that react with $C_8H_8$ in a kinetically relevant step to form styrene oxide. Measured activation enthalpies for $C_8H_8$ epoxidation with pore size among these materials (*e.g.*, Ti–$SiO_2$ (37 ± 4 kJ mol$^{-1}$) > Ti-FAU (22 ± 2 kJ mol$^{-1}$) > Ti-BEA (9 ± 2 kJ mol$^{-1}$)), which shows that the micropores of BEA enthalpically stabilize $C_8H_8$ epoxidation transition states relative to the Ti–OOH reactive intermediate. Apparent activation entropies, however, become increasingly negative with decreasing pore size (−155 to −234 J mol$^{-1}$ K$^{-1}$) suggesting that the dispersive interactions between $C_8H_8$ epoxidation transition states and the pore walls of BEA results in the significant loss of translational and vibrational entropy. Consequently, the greater rates and selectivities for $C_8H_8$ epoxidation within Ti-FAU arise from the balance of enthalpy–entropy compensation effects that depend on the pore structure of the silicate. The 1.2 nm voids of FAU give enthalpic benefits for $C_8H_8$ epoxidation, relative to Ti–$SiO_2$, yet does not incur the same entropic losses suffered within Ti-BEA. Collectively, these methods and data provide a pathway to synthesize Al-free M-FAU materials, from synthetic or natural Al-FAU, that can be used for adsorption, separations, or catalysis, and which can allow for the access of other Ti-zeolite structures through inter-zeolitic transformations.

# Experimental

### FAU dealumination and heteroatom incorporation

Heteroatom-substituted FAU (M-FAU) were prepared through the post-synthetic modification of $H^+$-form Al-FAU (Zeolyst, CBV 720; Si : Al ~ 15). Al-FAU was treated in $HNO_3$ (Macron Chemicals, 68–70 wt.%, 20 cm$^3$ $g_{Al\text{-}FAU}^{-1}$) at reflux for 18 hours with the intent to remove framework Al by forming soluble $Al(NO_3)_3$. The solids were recovered by vacuum filtration, washed with additional $HNO_3$ (5 cm$^3$ $g_{Al\text{-}FAU}^{-1}$), and deionized $H_2O$ (17.8 MΩ cm; 25 cm$^3$ $g_{Al\text{-}FAU}^{-1}$). Note that concentrated $HNO_3$ can easily cause chemical burns and should be handled carefully. These washed solids were then dried at 823 K (5 K min$^{-1}$) for 6 h in flowing air (Airgas, Ultra-zero grade; 100 cm$^3$ min$^{-1}$) to produce a partially-dealuminated FAU with a Si : Al of ~200 (estimated by energy dispersive X-ray fluorescence, see below). The partial dealumination may result from the redeposition of Al into the FAU framework during filtration at room temperature. To further remove Al atoms, these dried solids were then subjected to a second dealumination sequence identical to that described above to produce Si-FAU with a Si : Al greater than 900.

Ti and Sn atoms were incorporated into the FAU framework through the liquid-phase grafting of $TiCl_4$ (Sigma-Aldrich, 99.9%) or $SnCl_4{\cdot}5H_2O$ (Sigma-Aldrich, 98%) in dichloromethane (DCM, Fisher Chemicals, Certified ACS Stabilized, 25 cm$^3$ $g_{Si\text{-}FAU}^{-1}$). Nb- and Ta-substituted FAU were prepared by refluxing $Nb(OEt)_5$ (Sigma Aldrich, 99.95%) or $Ta(OEt)_5$ (Sigma-Aldrich, 99.98%) in isopropanol (Fisher Chemical, Optima, 25 cm$^3$ $g_{Si\text{-}FAU}^{-1}$). In all cases, the suspensions containing Si-FAU and $MCl_4$ or $M(OEt)_5$ were kept under an argon atmosphere using standard Schlenk technique for at least 6 h. Prior to introduction of the solvent and the $MCl_x$ or $M(OEt)_5$ precursor, the Si-FAU was dehydrated at 473 K under vacuum (<5 Pa) for 3 h to desorb any residual $H_2O$ that may hydrolyze the metal precursors. Dehydration of Si-FAU is particularly important when using the $TiCl_4$ precursor, which readily hydrolyzes to form

 

oligomeric and bulk $TiO_x$ aggregates. The solvent and other volatile components were removed *via* rotary evaporation and the recovered solids were heated in flowing air (100 $cm^3$ $min^{-1}$) to 823 K at 5 K $min^{-1}$ and held for 6 h to yield bright white-colored solids in all cases.

Titanium substituted BEA (Ti-BEA) and Ti-grafted $SiO_2$ (Ti–$SiO_2$) materials were used within a previous study,[23] which presents the detailed chemical and physical characterization of these materials. The titanium silicalite-1 (TS-1) material was synthesized according to the recommended procedure from the International Zeolite Association's Synthesis Commission to contain 0.3 wt% Ti.[46] The relevant characterization data is presented within the ESI† (section S1).

Briefly, Ti-BEA was prepared by the post-synthetic modification of commercial Al-BEA (Zeolyst, CP814E). Al-BEA was contacted with $HNO_3$ at reflux for 18 h with the intent of forming soluble $Al(NO_3)_3$. The solids were recovered by vacuum filtration and washed thoroughly with $H_2O$ prior to dehydration at 823 K (6 h; 5 K $min^{-1}$) in flowing air (100 $cm^3$ $min^{-1}$), which produced Si-BEA (Si : Al > 1200). Ti atoms were incorporated into Si-BEA through the liquid-phase incorporation of $TiCl_4$ in DCM at reflux. Volatile components were removed *via* rotary evaporation and recovered solids were treated at 823 K (5 K $min^{-1}$) for 6 h in flowing air (100 $cm^3$ $min^{-1}$) to produce Ti-BEA.

Ti–$SiO_2$ was synthesized through the grafting of titanium 1,3-dimethoxy-*tert*-butylcalix[4]arene (Ti-dmcalix) onto $SiO_2$ (Selecto Scientific, 32–62 μm particle size, 5.4 nm pore diameter) through reflux in toluene in an Ar atmosphere.[23] Prior to grafting, $SiO_2$ was dehydroxylated at 573 K under vacuum (<5 Pa) for 10 h to produce isolated SiOH and minimize any Ti–O–Ti oligomer formation. Ti-dmcalix-Grafted $SiO_2$ was recovered by vacuum filtration and treated at 823 K (5 K $min^{-1}$) for 6 h in air (100 $cm^3$ $min^{-1}$) to produce Ti–$SiO_2$.

TS-1 was synthesized hydrothermally in hydroxide media. In short, 150 mg of titanium(IV) butoxide (TBOT; Sigma-Aldrich, 97%) was dissolved in 27.7 g of tetraethylorthosilicate (TEOS; Sigma-Aldrich, 98%) in a polypropylene container to form a homogeneous solution and was subsequently cooled to 273 K. Separately, a mixture of 28.7 g of tetrapropylammonium hydroxide (TPAOH; Sachem, 40% in $H_2O$) and 50.5 g of $H_2O$ was cooled to 273 K and was slowly added (over ~1 min) to the solution of TBOT and TEOS, which yielded a biphasic mixture. This solution was then warmed to 298 K and stirred for 12 h to produce a homogeneous solution, which indicates complete hydrolysis of the TBOT and TEOS. The cover was then removed to evaporate the ethanol and butanol formed through hydrolysis and produce a solution with the approximate composition of 1 Si : 0.0033 Ti : 0.43 TPAOH : 28.3 $H_2O$. This solution was then loaded into a Teflon-lined stainless-steel autoclave (Parr instruments, 125 $cm^3$) that contained 5% (relative to $SiO_2$ in the gel) TS-1 from a previous synthesis. This autoclave was heated to 443 K while rotating (30 rpm) in a convection oven for 3 days. The resulting solids were recovered by centrifugation, washed with $H_2O$, and dried for 16 h at 373 K. The dried solids were then heated in flowing air (100 $cm^3$ $min^{-1}$) at 823 K (1 K $min^{-1}$) for 10 h to produce TS-1.

### Catalyst characterization

The metal contents of all M-FAU were determined using energy dispersive X-ray fluorescence. Finely-ground M-FAU samples were loaded into a polypropylene sample holder (2.45 cm aperture) which was sealed with ultralene film. These samples were loaded into a spectrometer (Shimadzu, EDX-7000) whose sample chamber was purged with He (Airgas, Ultra-zero grade) prior to measurement. Spectra were obtained between 0 and 30 keV (500 scans), and the relative intensities of the element-specific fluorescence features and their associated calibration factors were used to determine the percent, by mass, of each element within the sample.

The crystallinity and contraction/expansion of the FAU framework was measured through X-ray diffraction. Samples were loaded onto a polypropylene holder and X-ray diffractograms were collected on a diffractometer (Siemens/Bruker, D5000) with Cu Kα radiation (0.15418 nm) under ambient conditions.

The surface area and pore-size distributions of M-FAU were determined by $N_2$ adsorption. Gas-phase $N_2$ adsorption isotherms (77 K) were collected on a volumetric adsorption instrument (Micromeritics, 3Flex). Samples (50–100 mg) were pelletized and sieved to retain particles between 250 and 500 μm in diameter. These samples were degassed by heated under vacuum (<0.7 Pa, 673 K) for 6 h prior to adsorption measurements. Pore size distributions were determined from $N_2$ adsorption isotherms using a cylindrical pore model with non-local density functional theory (NLDFT) in the 3Flex software.

The presence of highly-disperse M atoms (and absence of bulk or oligomeric $MO_x$ domains) was inferred by the band edge energies, which were measured using diffuse reflectance UV-vis spectroscopy. Total reflectance spectra were measured under ambient conditions using a diffuse-reflectance accessory (Harrick, Cricket) with a UV-vis-NIR spectrophotometer (Agilent, CARY 5). Prior to measurement, samples were intimately mixed with magnesium oxide (MgO; Sigma-Aldrich, 99.995%) in a 1 : 10 ratio by mass.

Infrared (IR) spectra of adsorbed pyridine (Sigma-Aldrich, 99.8%) were used to confirm the presence of Lewis acid sites within M-FAU and to detect Brønsted acid sites associated with remaining framework Al atoms. IR spectra (128 scans, 4 $cm^{-1}$) were obtained at equilibrium pyridine coverages using a custom-built temperature-controlled transmission cell coupled to a Fourier-transform IR spectrometer (Bruker, Tensor 37) with a liquid $N_2$-cooled HgCdTe detector. Thin catalyst pellets (~45 mg) were loaded into the transmission cell, which was configured with $CaF_2$ windows and connected to a gas manifold equipped with a liquid-injection port. All

materials were first heated to 573 K (10 K $min^{-1}$) and held for >2 h in flowing He (50 $cm^3$ $min^{-1}$) to desorb any volatile compounds. Pyridine was introduced using a syringe pump (KD Scientific, Legato 100) and vaporized in the gas-transfer lines into a stream of He (50 $cm^3$ $min^{-1}$) to contact the M-FAU pellets.

The fraction of Si atoms that exist as $Si(OSi)_3OH$ ($\phi_{NMR}$) within M-FAU samples were determined using $^{29}Si$ magic angle spinning-nuclear magnetic resonance (MAS-NMR) spectroscopy. MAS-NMR spectra (4000 scans) were collected on a spectrometer (Varian, Unity Inova 300 MHz; 7.05 T), operating at 59.6 MHz Larmor frequency, equipped with a 4 mm MAS probe (Varian-Chemagnetics, double-resonance HX, APEX) under ambient conditions. M-FAU samples (~70 mg) were loaded into 4.0 mm outer diameter zirconia rotors that were spun at 10 kHz. Powdered octakis(trimethylsiloxy)-silsesquioxane ($Q_8M_8$) was used for $^{29}Si$ chemical shift referencing ($Q_8M_8$ has a chemical shift of 11.45 ppm relative to tetramethylsilane (TMS) at 0 ppm). Pulse width calibration was performed on Si-FAU, which yielded a 90° pulse width of 1.5 μs. The recycling delay ($d_1$) for SI-FAU was varied between 5 and 15 s to determine how $\phi_{NMR}$ changed with $d_1$; a $d_1$ of 10 s was used for all M-FAU as $\phi_{NMR}$ was identical for a $d_1$ of 10 and 15 s.

### Measurement of epoxidation rates

For all kinetic measurements, a Ti-FAU sample with 0.3 wt% Ti atoms was used to avoid artifacts from internal mass-transfer restrictions. Rates of styrene ($C_8H_8$; Sigma-Aldrich, 99%) and 2,4-dimethylstyrene ($C_{10}H_{12}$; Sigma-Aldrich, 97%) epoxidation were measured in batch reactors (100 $cm^3$, three-neck round bottom flasks) equipped with reflux condensers to minimize evaporative losses. Solutions of $C_8H_8$ or $C_{10}H_{12}$ and $H_2O_2$ (Fisher; 30 wt% in $H_2O$) with benzene (internal standard; Sigma-Aldrich, >99% thiophene-free) in acetonitrile (Fisher Chemicals, HPLC grade) was heated to the desired temperature (308–348 K) while stirring at 700 rpm. Epoxidation was initiated by the introduction of Ti-FAU and small aliquots were extracted as a function of time through a 0.22 μm syringe filter. The concentrations of all organic components within these aliquots were determined using a gas chromatograph (HP, 5890 Series A) equipped with a flame-ionization detector. The concentration of $H_2O_2$ in each aliquot was determined by colorimetric titration using aqueous $CuSO_4$ (8.3 mM, Sigma-Aldrich, >98%) indicator with neocuproine (12 mM, Sigma-Aldrich, >98%) and ethanol (25% v/v, Decon Laboratories, 100%).[47] Notably, styrene oxidation results in the formation of styrene oxide ($C_8H_8O$) and phenylacetaldehyde. Extrapolation of the selectivity towards each of these species to the limit of zero conversion shows that phenylacetaldehyde forms by $C_8H_8O$ isomerization. Here, the combined concentrations of $C_8H_8O$ and phenylacetaldehyde were used to calculate the turnover rates for epoxidation reactions.

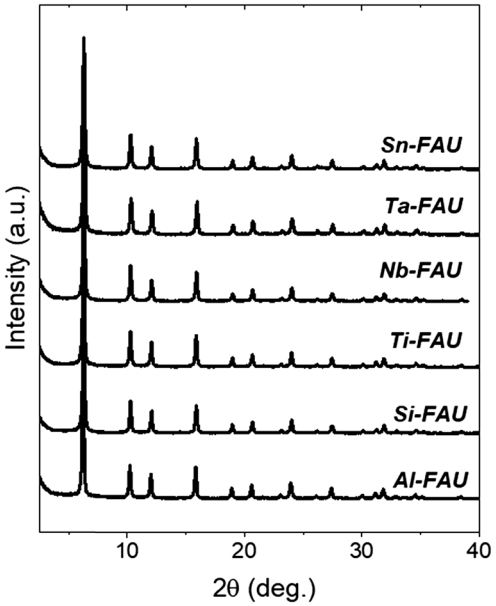


**Fig. 1** X-ray diffractograms for Al-, Si-, Ti-, Nb-, Ta-, and Sn-FAU. Diffractograms are vertically offset for clarity.

## Results and discussion

### Crystallinity of FAU maintained during post-synthetic modification

Titanium, niobium, tantalum, and tin framework-substituted FAU (M-FAU) were synthesized through the post-synthetic modification of $H^+$-form Al-FAU. Fig. 1 shows X-ray diffractograms for M-FAU all possess features indicative of the FAU framework. The relative crystallinity for each M-FAU was estimated by taking the ratio of the 10.3° and 6.3° and assuming 100% crystallinity within Al-FAU. There is no apparent loss in crystallinity upon post-synthetic modification (Table 1), which suggests that dealumination and subsequent metal substitution does not alter the FAU framework. The $d_{111}$ spacing[20] shifts from 6.23° to 6.28° (Fig. S3†) upon dealumination, which is consistent with the contraction of the FAU framework resulting from appreciable densities of silanol nests ($(SiOH)_4$). The incorporation of heteroatoms shifts the $d_{111}$ spacing to 6.24° (in the case of Ti), which indicates that the M atoms are integrated into the $(SiOH)_4$ nests formed by dealumination to produce framework heteroatoms sites with the capacity for catalysis.

### Post-synthetic modification does not form mesopores

Nitrogen adsorption isotherms (77 K; Fig. 2a) were measured on Al-, Si-, and Ti-FAU to probe changes in the physical properties (*i.e.*, Brunauer–Emmett–Teller (BET) surface area, pore-size distribution) of the FAU framework upon dealumination and subsequent Ti-atom incorporation. The adsorption profile for $N_2$ is characteristic of weak adsorbate–adsorbent interactions (type III) and approaches micropore filling below a relative pressure ($P/P_0$) of $10^{-4}$.[48] As $P/P_0$ is increased, $N_2$ adsorption resembles a typical type I isotherm

**Table 1** Si : Al and Si : M ratios, metal loadings, relative crystallinities, optical band gaps, BET surface areas, fraction of Si atoms existing as SiOH ($\phi_{NMR}$), and relative densities of hydrogen-bonded SiOH ($\phi_{IR}$) within M-FAU

| Sample | Si : Al[a] | Si : M[a] | Metal loading[a] (wt%) | Crystallinity[b] (%) | Band gap[c] (eV) | BET surface area[d] ($m^2\ g^{-1}$) | $\phi_{NMR}$[e] | $\phi_{IR}$[f] |
|---|---|---|---|---|---|---|---|---|
| Al-FAU | 14.8 | 14.8 | 2.85 | 100 | — | 800 | —[g] | —[h] |
| Si-FAU | >900 | — | — | 96 | — | 760 | 0.091 | 3.4 ± 0.2 |
| Ti-FAU | >900 | 39.1 | 1.97 | 106 | 4.4 | 740 | 0.051 | 2.1 ± 0.1 |
| Nb-FAU | >900 | 37.9 | 3.85 | 105 | 4.8 | — | 0.049 | 2.5 ± 0.2 |
| Ta-FAU | >900 | 47.3 | 5.90 | 108 | 4.8 | — | 0.055 | 2.7 ± 0.2 |
| Sn-FAU | >900 | 42.3 | 4.42 | 99 | 4.2 | — | 0.053 | 1.9 ± 0.1 |

[a] Measured by EDXRF. [b] Determined by DRUV-vis spectroscopy by extrapolating the linear portion of the leading edge of the corresponding Tauc plot (Fig. 3). [c] Estimated by taking the ratio of the intensity for the 10.3° to the 6.3° diffraction features and assuming perfect 100% crystallinity for Al-FAU. [d] Calculated using $N_2$ adsorption isotherms (Fig. 2a). [e] Quantified using $^{29}$Si MAS-NMR (Fig. 4). [f] Determined from FTIR spectra of dehydrated M-FAU (Fig. 5). [g] NMR features for Si atoms residing as $Si(OAl)(OSi)_3$ and $Si(OSi)_3OH$ overlap and precludes determination. [h] $\nu$(O–H) of $H^+$ bound to Si–O–Al moieties overlap with $\nu$(O–H) of hydrogen-bonded SiOH, which prevents quantification.

that is characteristic of adsorption within a microporous solid. Fig. 2a contains a log-scale for the abscissa that gives the illusion that $N_2$ adsorption resembles a type IV isotherm; however, the linear-scaling of $P/P_0$ (Fig. S4†) reveals the type 1 nature of $N_2$ adsorption. The surface area of M-FAU was estimated using BET theory[48] and yielded equivalent values for the three samples tested (740–800 $m^2\ g^{-1}$, Table 1), which further suggests that post-synthetic modification of Al-FAU does not modify the long-range order of the framework or create sufficiently large defects that change the internal surface area. Fig. 2b shows the pore-size distributions calculated for Al-, Si-, and Ti-FAU all possess a significant feature with a characteristic pore width of ~1.2 nm, which corresponds to the supercage within the FAU framework.[49] The small feature around 1.8 nm may result from defects that partially connect two adjacent cages. Importantly, the similarities between the pore-size distributions, the BET surface areas, and the characteristics of $N_2$ adsorption all suggest that post-synthetic modification does not significantly alter the FAU framework. Nitrogen possesses a significant quadrupolar moment that may lead to specific interactions with adsorption sites, which typically prompts the use of argon as an adsorptive.[48] The similarities between the adsorption isotherms here, however, further suggests the FAU framework is unchanged upon post-synthetic treatment.

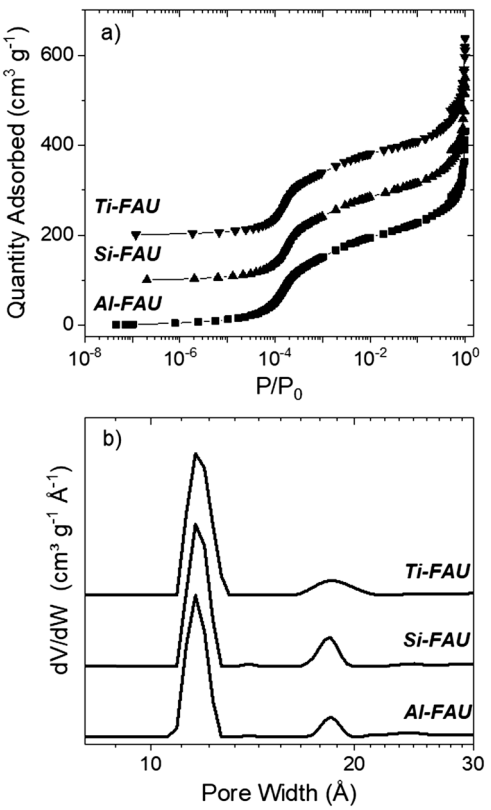


**Fig. 2** (a) Nitrogen adsorption isotherms (77 K; offset by 100 $cm^3\ g^{-1}$ for clarity) and (b) pore-size distributions for Al-FAU, Si-FAU, and Ti-FAU. The pore-size distributions were calculated using a cylindrical pore model with NLDFT. Pore-size distributions are normalized to the 1.15 nm feature and offset for clarity.

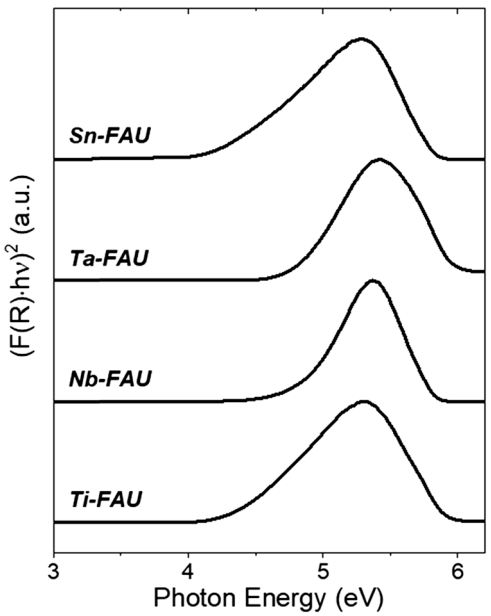


**Fig. 3** Tauc plots for Ti-, Nb-, Ta-, and Sn-FAU. Note that $F(R)$ corresponds to the Kubelka–Munk pseudo-absorbance. All spectra were normalized to the most-intense feature and are offset for clarity. Optical band gaps were calculated from regressing the linear portion of the leading edge to a value of zero.

### Metal sites within FAU framework are highly disperse

Optical band gaps reports on the speciation (and dispersion) of semi-conducting and insulating solids.[22,50,51] Fig. 3 shows Tauc plots for M-FAU all possess a single prominent absorbance feature between 5.1 and 5.3 eV, which corresponds to the ligand-to-metal charge transfer between the O atoms within the framework of FAU and the M atom within the sample (*e.g.*, charge transfer between the 2p orbitals of oxygen to the 3d orbitals of $Ti^{4+}$). Table 1 shows that the band gaps for these Ti-, Nb-, Ta-, and Sn-FAU are all significantly larger those of the bulk $MO_x$ analogues (bulk anatase $TiO_2$, $Nb_2O_5$, $Ta_2O_5$, and $SnO_2$ have band gaps of 3.2,[52] 3.4,[53] 3.9,[54] and 3.6 eV,[55] respectively). Moreover, the band gaps for these M-FAU samples are comparable to those for hydrothermally-synthesized M-BEA[16,24,56] and M-MFI[56–59] zeolites, which suggests these metal atoms are incorporated into the FAU framework. The large band gaps for the M-FAU within this study, relative to bulk $MO_x$, suggest that metal atoms are well isolated within the zeolite framework and that these samples contain negligible amounts of M–O–M linkages.

### Grafting of metal ions leads to reduction in the number of SiOH

The fraction of Si atoms that exist as SiOH within each M-FAU can provide indirect evidence for the formation and elimination of $(SiOH)_4$ upon dealumination and subsequent metal-ion incorporation. Fig. 4 shows $^{29}Si$ MAS-NMR spectra that contain distinct NMR features at chemical shifts of −107 and −100 ppm on all M-FAU. The feature at −107 ppm corresponds to Si atoms within the FAU framework coordinated to four siloxane functions (*i.e.*, $Si(OSi)_4$, denoted as $Q^4$ sites) or to three siloxanes and a substituted metal atom (*i.e.*, $Si(OSi)_3OM$; M = Ti, Nb, Ta, Sn).[28,60] Fig. S5b† shows the full width-half max of the $Q^4$ feature increases from 0.9 ppm for Si-FAU to 1.1–1.2 ppm for M-FAU, which indicates this feature contains contributions from both $Si(OSi)_4$ and $Si(OSi)_3OM$ moieties. The broad feature at −100 ppm for Al-FAU corresponds to Si atoms that possess an adjacent Al atom (*i.e.*, $Si(OAl)(OSi)_3$).[61] For all other M-FAU, the small feature at −100 ppm corresponds to Si atoms that possess a single pendant hydroxyl (*i.e.*, $Si(OSi)_3OH$, denoted as $Q^3$ sites).[62,63] The fraction of Si atoms that reside as $Si(OSi)_3OH$ ($\phi_{NMR}$) is described by the fraction of $Q_3$ sites to the sum of $Q^3$ and $Q^4$ sites

$$\phi_{NMR} = \frac{A_{Q^3}}{A_{Q^3} + A_{Q^4}} \quad (1)$$

where $A_{Q^3}$ and $A_{Q^4}$ are the areas of the deconvoluted $^{29}Si$ MAS-NMR features for $Q^3$ and $Q^4$ sites, respectively (section S3.1† shows representative peak fits to determine the $Q^3$ and $Q^4$ areas). Table 1 shows that $\phi_{NMR}$ decreases from 0.09 to 0.05 upon framework substitution into Si-FAU samples, which follows expectations based upon the liberation of HCl or EtOH upon metal grafting onto $(SiOH)_4$ and formation of Si–O–M linkages. A statistical distribution of $(SiOH)_4$ within the framework before and after the substitution of M atoms

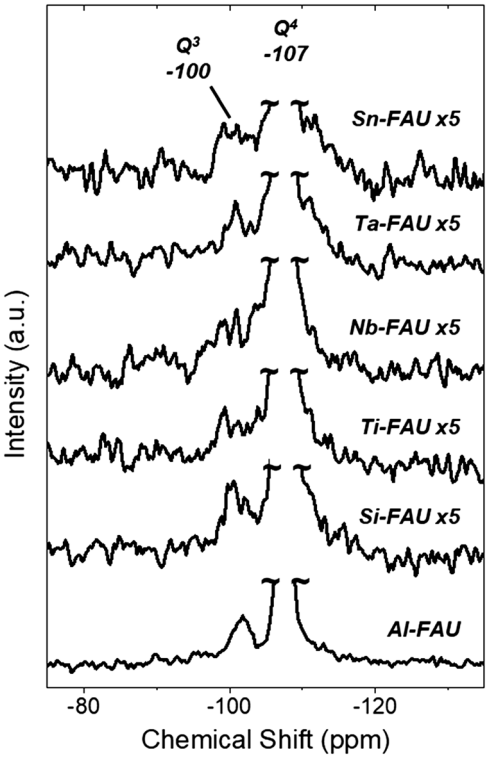


**Fig. 4** $^{29}Si$ direct polarization MAS-NMR spectra of Al-, Si-, Ti-, Nb-, Ta-, and Sn-FAU. Spectra are normalized to the $Q^4$ feature and scaled to the indicated value (*e.g.*, 5× magnification for Si-FAU). The intense $Q^4$ feature has been truncated and spectra are vertically offset for clarity. Fig. S5† shows $^{29}Si$ MAS-NMR spectra that includes the $Q^4$ feature.

(assuming a final Si : M ratio of ~40; Table 1) suggests a ~35% reduction in the total number of $(SiOH)_4$, which qualitatively agrees with the measured changes in $\phi_{NMR}$ between Si-FAU and M-FAU (~44% reduction). Values of $\phi_{NMR}$, however, do not directly represent the density of $(SiOH)_4$ (*i.e.*, SiOH formed upon dealumination), because these values encompass all Si atoms that exist as SiOH including those at point defects and on the external surface of FAU particles.

### Metal ions within M-FAU occupy $(SiOH)_4$ and are Lewis acidic

Isolated SiOH and hydrogen-bonded $(SiOH)_4$ moieties in M-FAU materials possess distinct $\nu$(O–H) that can be used to yield semiquantitative estimates for the relative density of $(SiOH)_4$ groups. Fig. 5 shows IR spectra of dehydrated M-FAU samples (573 K in He) all possess distinct features at 1990 and 1865 $cm^{-1}$, which correspond to $\nu$(Si–O–Si) overtones[19,64] that reflect contributions from the FUA framework. The complex broad features between 3750–3400 $cm^{-1}$ correspond to $\nu$(O–H) modes of distinct types of SiOH. The sharp feature at 3740 $cm^{-1}$ within all M-FAU corresponds to $\nu$(O–H) of isolated SiOH that do not interact with nearby hydrogen bond-acceptor moieties. Within Al-FAU, the sharp features at 3640 and 3550 $cm^{-1}$ are characteristic of Brønsted acid sites

 

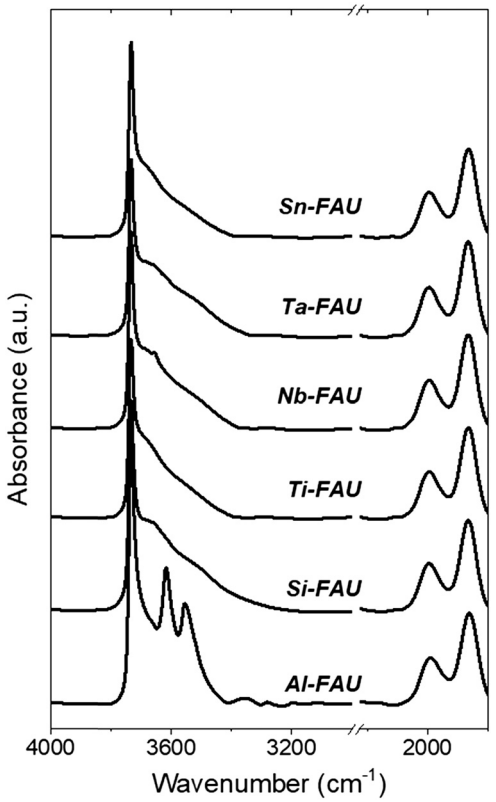


**Fig. 5** Infrared spectra of dehydrated Al-, Si-, Ti-, Nb-, Ta-, and Sn-FAU in flowing He (50 $cm^3$ $min^{-1}$, 573 K). Spectra have been normalized to $\nu$(Si–O–Si) at 1865 $cm^{-1}$ and are vertically offset for clarity.

within the supercage and sodalite cages of FAU, respectively.[65,66] The broad $\nu$(O–H) feature extending between 3750–3400 $cm^{-1}$ in M-FAU (M = Si, Ti, Nb, Ta, and Sn) samples corresponds to $(SiOH)_x$ (*e.g.*, $(SiOH)_4$) that contain adjacent hydrogen-bonded –OH groups.[24,67]

Relative densities of isolated SiOH and $(SiOH)_4$ among M-FAU samples are estimated by normalizing each infrared spectra to the total number of framework bonds, which is assumed to be constant among these samples and is represented by the intensity of the $\nu$(Si–O–Si) (1865 $cm^{-1}$) within this study. Peak fitting (section S3.2†) of the $\nu$(O–H) region allows for the deconvolution of isolated SiOH (3740 $cm^{-1}$) and $(SiOH)_4$ groups (3300–3740 $cm^{-1}$); where the ratio of the cumulative area of $\nu$(O–H) for $(SiOH)_4$ ($A_{(SiOH)_4}$) normalized to that of $\nu$(Si–O–Si) ($A_{Si-O-Si}$) yields a quantitative estimate for the relative density of $(SiOH)_4$ ($\phi_{IR}$) among M-FAU materials.

$$\phi_{IR} = \frac{A_{(SiOH)_4}}{A_{Si-O-Si}} \quad (2)$$

Table 1 shows values of $\phi_{IR}$ decrease from 3.4 ± 0.2 for Si-FAU to ~2 ± 0.1 for M-FAU. The decrease in $\phi_{IR}$ (~40%) for Ti- and Sn-FAU is quantitatively consistent with the expected loss of $(SiOH)_4$ (~35%) upon metal-atom incorporation. Nb- and Ta-FAU are pentacoordinate and possess a pendant –OH, which obviates how changes in $\nu$(O–H) solely result in the loss of $(SiOH)_4$; however, the general trend in decreasing $\phi_{IR}$ for these materials suggests the incorporation of Nb and Ta atoms into $(SiOH)_4$. Collectively, the data and interpretation from X-ray diffraction, diffuse reflectance, UV-vis, $N_2$ volumetric adsorption, $^{29}Si$ MAS-NMR, and IR spectroscopy experiments suggest that the post-synthetic modification procedure presented here first generates a nearly siliceous FAU material with a number of $(SiOH)_4$ nests equal to the original number of Al atoms, and second, substitutes the desired M atoms (M = Ti, Nb, Ta, Sn) into the zeolite framework.

Heteroatom-substituted zeolites often act as solid Lewis acid catalysts, where the efficacy of these materials depends strongly on the electron affinity (described colloquially as the "Lewis acid strength") of the active site.[13,18,22,23,56] Pyridine molecules bound to Brønsted acid sites form pyridinium ions that possess vibrational modes distinct from pyridine molecules bound to Lewis acid sites, and these differences provides a means to discriminate between different types of acid sites within solid materials. Fig. 6 shows IR spectra of M-FAU materials in contact with dilute streams of vapor-phase pyridine (0.25 kPa, 101 kPa He, 473 K). All M-FAU

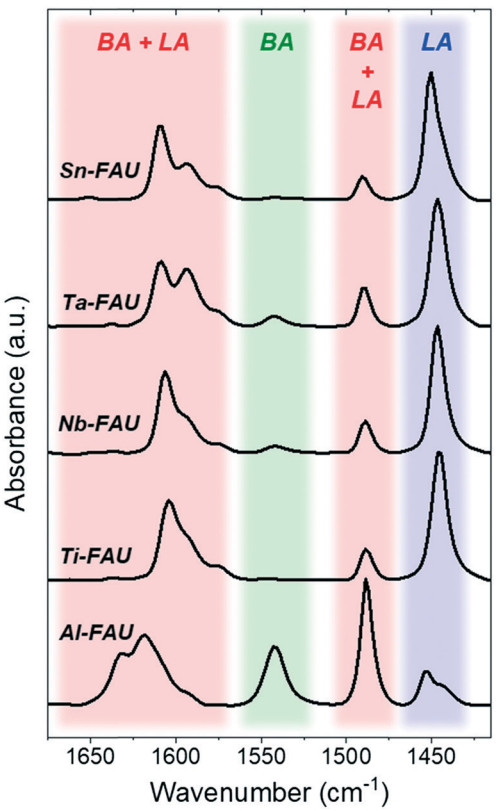


**Fig. 6** Infrared spectra of Al-FAU, Ti-FAU, Nb-FAU, Ta-FAU, and Sn-FAU in contact with gaseous pyridine (0.25 kPa, 101 kPa He, 473 K). All spectra were normalized to the most-intense feature between 1700–1400 $cm^{-1}$ and are offset for clarity. Colored regions correspond to expected regions for vibrational modes of pyridine coordinated to Lewis acid sites (LA; blue), Brønsted acid sites (BA; green), and both Brønsted and Lewis acid sites (BA + LA; red).

possess significant absorbance features between 1650–1575 $cm^{-1}$ and at 1500 $cm^{-1}$, which correspond to vibrational modes of pyridine molecules adsorbed to either Brønsted or Lewis acid sites.[68,69] The absorbance features around 1450 $cm^{-1}$ are assigned to the vibrational modes of pyridine adsorbed solely to Lewis acid sites, while the absorbance feature at 1540 $cm^{-1}$ is attributed to the vibrational modes of the pyridinium ion. Al-FAU clearly possesses the greatest density of Brønsted acid sites among these materials. Within Ti-, and Sn-FAU the feature at 1540 $cm^{-1}$ is nearly indistinguishable from baseline, which suggests these materials do not possess spectroscopically-observable densities of Brønsted acid sites. Fig. 6 shows that Nb- and Ta-FAU possess significant amounts of adsorbed pyridinium, because Nb and Ta atoms within zeolites are five coordinate and possess a pendant –OH,[70,71] which may act as a Brønsted acid. Notably, the presence of Brønsted acid sites within Nb- and Ta-FAU cannot be due to residual Al atoms, as the vibrational features that discriminate these features are not present on Ti- or Sn-FAU, which were synthesized using the same batch of Si-FAU. For all M-substituted FAU, there is a significant increase in intensity for absorbance features that correspond to pyridine bound to Lewis acid sites, which is consistent with reports for these metal atoms substituted into other silicate frameworks.[20,23,38,72] These Lewis acidic active sites constitute an important class of catalysts for a variety of reactions (see above), and the stabilization of intermediates critical to epoxidation catalysis within the FAU framework is demonstrated on Ti-FAU in the following section.

### Reaction pathways for alkene epoxidation with hydrogen peroxide

Zeolites and mesoporous silicates bind reactants by charge transfer at active sites but also permit the selective stabilization of surface intermediates through combinations of van der Waals and specific interactions among the extended zeolite surface, the solvent molecules and the reactive species. The extent of stabilization depends on both the size and shape of the confining pore and the reactive species contained within these spaces. Fig. 7 shows turnover rates for styrene ($C_8H_8$) epoxidation with hydrogen peroxide ($H_2O_2$) are significantly greater on Ti-FAU (1.2 nm supercage) than for Ti-BEA (0.65 nm pore) and Ti–$SiO_2$ (5.4 nm pore) at all reaction conditions examined. Specifically, epoxidation rates over Ti-FAU are greater than Ti-BEA and Ti–$SiO_2$ by factors of 2 and 7, respectively. $H_2O_2$ selectivities represent the percent of $H_2O_2$ molecules that are consumed by epoxidation reaction pathways and decrease in the same fashion as epoxidation turnover rates between Ti-FAU (47%), Ti-BEA (30%), and Ti–$SiO_2$ (6%). Rates of $H_2O_2$ decomposition (2.7 ± 0.9 (mmol $H_2O_2$)(mol Ti × s)) are nearly identical on Ti-FAU, Ti-BEA, and Ti–$SiO_2$ because the transition states for $H_2O_2$ decomposition are too small to experience interactions with the pore walls of the silicate hosts that differ among these materials. The importance of ultralow Al contents is

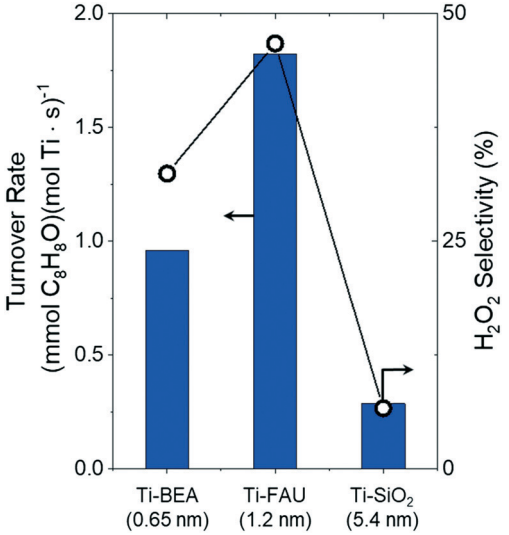


Fig. 7 Turnover rates for $C_8H_8$ epoxidation (blue bars) and $H_2O_2$ selectivities towards epoxidation products (black ○) over Ti-BEA, Ti-FAU, and Ti–$SiO_2$ with the characteristic pore dimension indicated. All reactions were run at standard conditions that lead to rates that are proportional to $C_8H_8$ concentrations (0.01 M $C_8H_8$, 0.01 M $H_2O_2$ in $CH_3CN$, 313 K).

exemplified in reactions that include Al-FAU to simulate a Si : Al of 150. The presence of Al-FAU results in no measurable $C_8H_8O$ formation; yet, rather forms 1-phenyl-1,2-ethanediol (from $C_8H_8O$ ring opening) and 1-phenylethanol (from $C_8H_8$ hydration over $H^+$ sites). Therefore, the differences in $C_8H_8$ epoxidation catalysis and the corresponding $H_2O_2$ selectivity must relate to how the stability of $C_8H_8$-derived intermediates depend on the characteristics of the Ti-silicate catalyst.

Turnover rates for ($C_8H_8$) epoxidation with hydrogen peroxide ($H_2O_2$) were measured as a function of $C_8H_8$ and $H_2O_2$ concentration to provide insight as to the mechanism for alkene epoxidation and reconcile the differences in rates and selectivities for $C_8H$ epoxidation. Notably, the Ti-FAU sample used within these kinetic measurements was synthesized to contain 0.3%, by weight, Ti atoms to avoid artifacts that may arise from internal concentration gradients (*i.e.*, to satisfy the Madon–Boudart criterion).[73] Fig. 8 shows that Ti-FAU, Ti-BEA, and Ti-FAU all possess nearly indistinguishable dependencies on the concentrations of $C_8H_8$ (Fig. 8a) and $H_2O_2$ (Fig. 8b) despite significant differences between the topologies of these silicate frameworks.

All Ti-based catalysts exhibit two kinetic regimes that differ in how epoxidation rates depend on the concentrations of reactants. At low $[C_8H_8]:[H_2O_2]$ (<1), turnover rates increase linearly with $[C_8H_8]$ and do not vary with $[H_2O_2]$ (when $[H_2O_2]$ is $>5 \times 10^{-3}$ M), which suggests that active sites are saturated with reactive species derived from $H_2O_2$ (*e.g.*, Ti–OOH). At low values of $[H_2O_2]$ ($<5 \times 10^{-3}$ M), turnover rates over Ti-BEA and Ti-FAU show a first-order dependence on both $[C_8H_8]$ and $[H_2O_2]$, which suggests that active sites are saturated with solvent molecules, rather than an intermediate derived from the reactants. At high

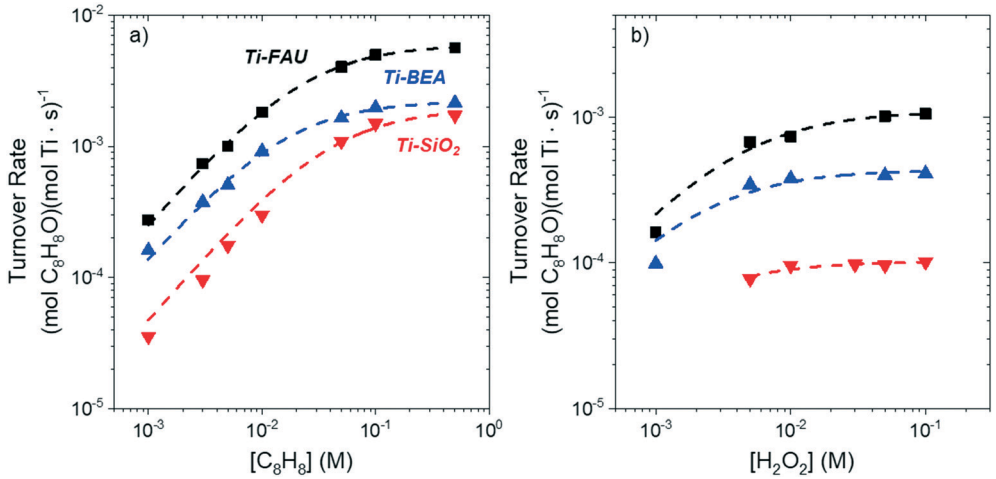


**Fig. 8** Turnover rates for $C_8H_8$ epoxidation as a function of (a) $[C_8H_8]$ (0.01 M $H_2O_2$) and (b) $[H_2O_2]$ ($3 \times 10^{-3}$ M $C_8H_8$) on Ti-FAU (black ■), Ti-BEA (blue ▲), and Ti–$SiO_2$ (red ▼) in $CH_3CN$ at 313 K. Dashed lines represent fits to eqn (4). Data for Ti-BEA and Ti–$SiO_2$ are adapted from ref. 23. Errors in $C_8H_8O$ formation rates are <10% and error bars are omitted for clarity.

$[C_8H_8]:[H_2O_2]$ (>10), turnover rates are independent of $[C_8H_8]$, indicating that the identity of the most abundant reactive intermediate (MARI) under these conditions is derived from $C_8H_8$ (*e.g.*, styrene oxide; $C_8H_8O$). The dependence of $C_8H_8O$ formation on reactant concentrations are identical with prior findings within our group for the epoxidation of cyclohexene,[21,22] styrene,[23] 1-octene,[24] and sulfoxidation of 2,5-dimethylthiophene[51] over groups 4 and 5-substituted zeolite BEA.

Scheme 1 shows a series of elementary steps that account for the measured effects of $[C_8H_8]$ and $[H_2O_2]$ on the rates of $C_8H_8O$ formation. This proposed catalytic cycle involves the quasi-equilibrated adsorption of $C_8H_8$ (step 1) and $H_2O_2$ (step 2) followed by the irreversible activation of $H_2O_2$ (step 3) to form Ti–OOH surface intermediates.[22,23] These Ti–OOH intermediates then react with $C_8H_8$ (step 4) or $H_2O_2$ (step 6) through rate-determining processes to form Ti-bound $C_8H_8O$ or $H_2O_2$-decomposition products, respectively. Finally, $C_8H_8O$

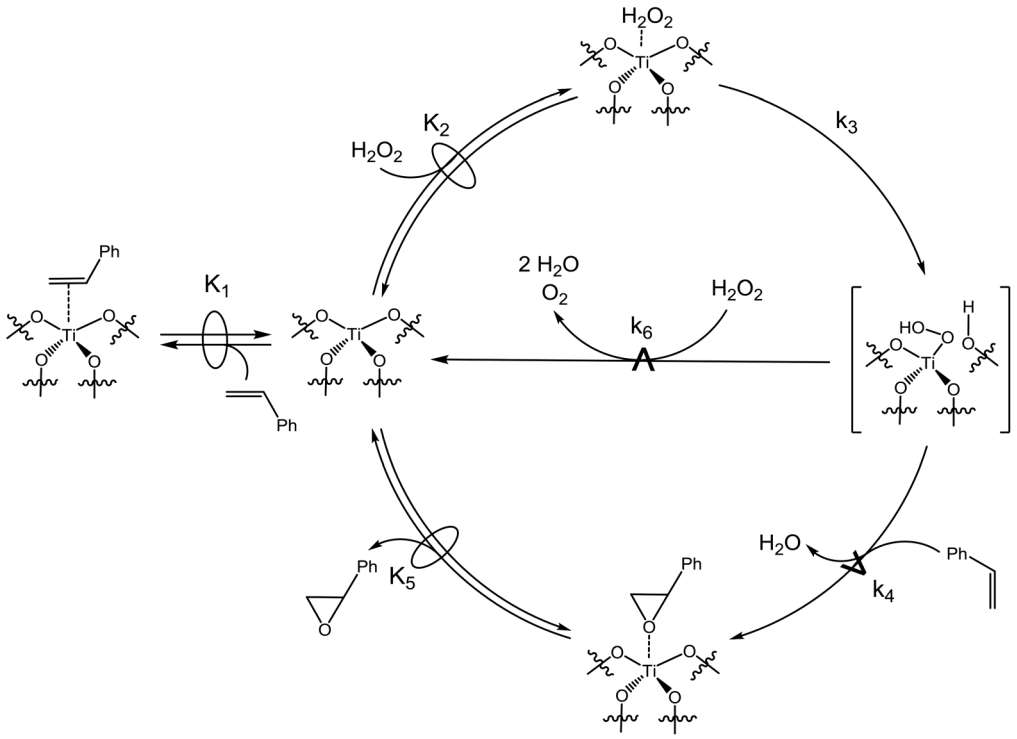


**Scheme 1** Proposed series of elementary steps for the epoxidation of $C_8H_8$ over Ti-based catalysts. The symbol ⇄ represents a quasi-equilibrated step, while ⇀ represents a kinetically relevant step.

molecules desorption is quasi-equilibrated and reforms the Ti active site.[23] Rates of $C_8H_8O$ formation ($r_E$) are given by

$$r_E = k_4[C_8H_8][\text{Ti–OOH}] \quad (3)$$

where $k_i$ is the rate constant for step I in Scheme 1 and [Ti–OOH] is the number of Ti–OOH surface intermediates. Application of the pseudo steady-state hypothesis to Ti–OOH surface intermediates, combined with a site balance over all possible configurations for surface intermediates bound to Ti active sites, yields

$$\frac{r_E}{[L]} = \frac{\frac{k_3k_4K_2[C_8H_8][H_2O_2]}{k_4[C_8H_8]+k_6[H_2O_2]}}{1+K_1[C_8H_8]+K_2[H_2O_2]+\frac{k_3K_2[H_2O_2]}{k_4[C_8H_8]+k_6[H_2O_2]}+\frac{[C_8H_8O]}{K_5}} \quad (4)$$

where $K_i$ is the equilibrium constant for step I, $[L]$ is the total number of Ti atoms loaded into the reactor, and the five terms within the denominator correspond to Ti active sites that are occupied by solvent molecules, adsorbed $C_8H_8$, adsorbed $H_2O_2$, Ti–OOH intermediates, and adsorbed $C_8H_8O$, respectively.

Reaction conditions where turnover rates depend linearly on $[C_8H_8]$ and are independent of $[H_2O_2]$ result in active sites that are saturated with Ti–OOH intermediates and reduces eqn (4) to yield

$$\frac{r_E}{[L]} = k_4[C_8H_8] \quad (5)$$

which matches the experimental observations within Fig. 8 at low $[C_8H_8]$:$[H_2O_2]$. Eqn (4) reproduces the measured dependence on $[C_8H_8]$ at high $[C_8H_8]$:$[H_2O_2]$ when two conditions are met. First, the formation of appreciable concentrations of $C_8H_8O$ results in the competitive adsorption of epoxide products, which has been observed for the binding of epoxide products to Lewis acidic Ti atoms within Ti-BEA[22–24] and TS-1.[74] Second, at high $[C_8H_8]$, values of $k_4[C_8H_8]$ become much greater than $k_6[H_2O_2]$ which reduces eqn (4) to

$$\frac{r_E}{[L]} = \frac{k_3K_2K_5[H_2O_2]}{[C_8H_8O]} \quad (6)$$

Eqn (6) is consistent with the independence of epoxidation turnover rates on $[C_8H_8]$ at high $[C_8H_8]$:$[H_2O_2]$ within Fig. 8a. Despite the indistinguishable mechanisms between Ti-FAU, Ti-BEA, and Ti–$SiO_2$, there are significant differences in the magnitude of the rates of epoxidation (*e.g.*, a factor of ~10 difference between Ti-FAU and Ti–$SiO_2$). To understand the origin of these differences, equitable comparisons of turnover rates and apparent activation enthalpies and entropies must be made at conditions that result in comparable coverages of surface intermediates.

### Thermochemical analysis shows transition state stabilization

Transition state theory postulates that the rate of reaction depends on the stability of an activated complex (*i.e.*, a transition state) relative to the stability of the stable intermediate immediately preceding it along a reaction trajectory (Scheme 2).[75] In the context of alkene epoxidation, Ti–OOH–$C_8H_8^{\ddagger}$ represents the transition state for $C_8H_8$ epoxidation which forms transiently upon reaction between Ti–OOH reactive intermediates with proximate $C_8H_8$.

$$Ti-OOH + C_8H_8 \overset{K_E^{\ddagger}}{\rightleftharpoons} Ti-OOH-C_8H_8^{\ddagger}$$

**Scheme 2** Proposed equilibrium for the formation of Ti–OOH–$C_8H_8^{\ddagger}$ from Ti–OOH and $C_8H_8$.

Within the tenets of transition state theory, turnover rates for $C_8H_8$ epoxidation, under conditions that result in Ti–OOH MARI, are given by

$$\frac{r_E}{[L]} = \frac{k_BT}{h}K_E^{\ddagger}[C_8H_8] \quad (7)$$

where $k_B$ is the Boltzmann constant, $h$ is Planck's constant, $T$ is the absolute temperature, and $K_E^{\ddagger}$ is the transition state equilibrium constant for epoxidation. $K_E^{\ddagger}$ depends on the thermodynamic stability of the transition state relative to the reference state and takes the form

$$K_E^{\ddagger} = e^{\frac{-\left(\Delta H_{App}^{\ddagger} - T\Delta S_{App}^{\ddagger}\right)}{RT}} \quad (8)$$

where $\Delta H_{App}^{\ddagger}$ and $\Delta S_{App}^{\ddagger}$ are the apparent activation enthalpy and entropy for epoxidation, respectively.

Fig. 9 shows $K_E^{\ddagger}$ as a function of inverse temperature for Ti-FAU, Ti-BEA, and Ti–$SiO_2$ used to determine the $\Delta H_{App}^{\ddagger}$ and $\Delta S_{App}^{\ddagger}$. Table 2 shows $\Delta H_{App}^{\ddagger}$ and $\Delta S_{App}^{\ddagger}$ both $C_8H_8$ epoxidation

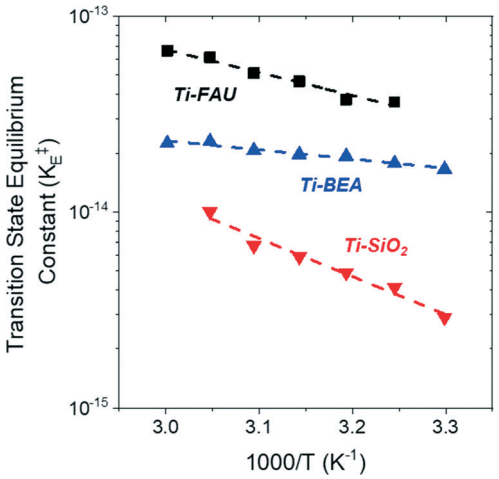


**Fig. 9** Transition state equilibrium constants for the formation of Ti–OOH–$C_8H_8^{\ddagger}$ as a function of inverse temperature over Ti-FAU (black ■), Ti-BEA (blue ▲), and Ti–$SiO_2$ (red ▼) under conditions that result in Ti–OOH MARI ($3 \times 10^{-3}$ M $C_8H_8$, 0.01 M $H_2O_2$ in $CH_3CN$). Dashed lines represent fits to eqn (8) (*i.e.*, the Eyring equation), whose slopes and intercepts are proportional to $\Delta H_{App}^{\ddagger}$ and $\Delta S_{App}^{\ddagger}$, respectively.

**Table 2** Apparent activation enthalpies and entropies for $C_8H_8$ epoxidation over Ti-FAU, Ti-BEA, and Ti-FAU under reaction conditions that result in a Ti–OOH saturated surface

| Catalyst | $\Delta H^{\ddagger}_{App}$ (kJ mol$^{-1}$) | $\Delta S^{\ddagger}_{App}$ (J mol$^{-1}$ K$^{-1}$) |
|---|---|---|
| Ti-FAU | 22 ± 2 | −185 ± 15 |
| Ti-BEA | 9 ± 2 | −234 ± 20 |
| Ti–$SiO_2$ | 37 ± 4 | −155 ± 15 |

obtained under reaction conditions that result in Ti–OOH saturated surfaces and in the absence of mass-transfer restrictions. Values of $\Delta H^{\ddagger}_{App}$ increase in the order of Ti-BEA < Ti-FAU < Ti–$SiO_2$, which suggests that the smaller pores of the *BEA framework (~0.65 nm) enthalpically stabilize the transition state for $C_8H_8$ epoxidation relative to FAU (1.2 nm) and $SiO_2$ (5.4 nm). This stabilization results from the solvation of Ti–OOH–$C_8H_8^{\ddagger}$ from the pore walls of the silicate support. The great extent of confinement of $C_8H_8$ epoxidation transition states within the voids of the Ti-catalyst, however, results in a disproportionate entropy of activation, where epoxidation within Ti-BEA incurs the greatest entropic loss, followed by Ti-FAU and Ti–$SiO_2$. This entropy of activation primarily reflects the loss of translational motion from fluid-phase $C_8H_8$ upon adsorption and formation of Ti–OOH–$C_8H_8^{\ddagger}$. For example, within Ti–$SiO_2$, the mesopore surrounding the Ti active site allows for the greatest flexibility of the $C_8H_8$ transition state, which results in the smallest loss of entropy among these three catalysts. Epoxidation within Ti-FAU results in intermediate values of $\Delta H^{\ddagger}_{App}$ and $\Delta S^{\ddagger}_{App}$, which results in favorable enthalpic stabilization due to the surrounding supercage relative to Ti–$SiO_2$; yet, provides enough flexibility for Ti–OOH–$C_8H_8^{\ddagger}$ as compared to Ti-BEA. Ti–$SiO_2$ possesses a greater dependence on temperature than Ti-FAU, which suggests that at a high enough temperature the rates should be greater on Ti–$SiO_2$. The isokinetic point (*i.e.*, the temperature at which the rates of $C_8H_8$ epoxidation are equal) between Ti-FAU and Ti-FAU, however, lies outside the solvent temperature window ($CH_3CN$ has a boiling point of 82 °C at atmospheric pressure), such that Ti-FAU will always possess a greater rate than Ti–$SiO_2$ within these types of reactors. Additional evidence for the selective stabilization of bulky aromatic transition states (*i.e.*, for 2,4-dimethylstyrene) within Ti-FAU relative to other Ti-silicates is provided within section S4.† In the context of this study, $C_8H_8$ can be thought of as a proverbial "Goldilocks," while Ti-FAU is the optimal "bear's bed."

## Conclusions

Multiple treatments of Al-FAU (Si : Al = 15) in $HNO_3$ removes nearly all of the Al atoms to produce siliceous FAU (Si : Al > 900). These treatments are necessary to remove the adventitious Al atoms, that may act as deleterious sites during zeolite catalysis (*e.g.*, within sugar isomerization, alcohol upgrading, alkene epoxidation). The liquid-phase grafting of metal chlorides and alkoxides leads to the isomorphic substitution of metal (M = Ti, Nb, Ta, Sn) atoms into the framework of FAU. Ti-FAU catalysts efficiently activate $H_2O_2$ to form Ti–OOH intermediates that are active for alkene epoxidation. In the case of styrene epoxidation, Ti-FAU possesses rates of epoxidation that are greater than Ti-BEA and Ti–$SiO_2$ by factors of 2 and 7, respectively. Rates of $H_2O_2$ decomposition, however, are invariant with the characteristic pore diameter of the Ti-silicate catalyst. Differences in catalysis are not due to differences in the mechanism for epoxidation; yet, reflect differences in the stability of the transition states for $C_8H_8$ epoxidation. Specifically, $C_8H_8$ epoxidation transition states are enthalpically stabilized within Ti-FAU relative to Ti–$SiO_2$ and also possess greater entropic freedom than within Ti-BEA, which results in the lowest free energies within the bounds of solvent stability. The work presented here serves as an exemplary example for how zeolite framework topology can be chosen to selectively stabilize desired surface intermediates. The synthetic protocols established here will enable the design of new materials in the quest for the rational development of catalysts.

## Conflicts of interest

D. T. B. and D. W. F. are inventors on a patent application (U.S. Patent Application No. 62/944,412 (2019)) for the synthesis and application of M-FAU, submitted by the University of Illinois at Urbana-Champaign.

## Acknowledgements

We thank Dr. Nicholas Thornburg and Prof. Justin Notestein for synthesizing Ti–$SiO_2$. D. T. B. was supported by the Department of Defense through the National Defense Science & Engineering Graduate Fellowship (NDSEG) Program. This work was carried out, in part, in the Frederick Seitz Materials Research Laboratory Central Research Facilities and the School of Chemical Sciences NMR Lab at the University of Illinois. This work was supported by the U.S. Army Research Office (W911NF-19-1-0100) and Department of Energy (DE-SC0020224).

## Notes and references

1 C. Li, C. Paris, J. Martínez-Triguero, M. Boronat, M. Moliner and A. Corma, *Nat. Catal.*, 2018, **1**, 547–554.
2 A. Corma, M. A. Camblor, P. Esteve, A. Martínez and J. Perez-Pariente, *J. Catal.*, 1994, **145**, 151–158.
3 C. B. Dartt and M. E. Davis, *Appl. Catal., A*, 1996, **143**, 53–73.
4 C. B. Khouw, C. B. Dartt, J. A. Labinder and M. E. Davis, *J. Catal.*, 1994, **149**, 195–205.
5 R. Gounder and M. E. Davis, *AIChE J.*, 2013, **59**, 3349–3358.
6 G. Noh, Z. Shi, S. I. Zones and E. Iglesia, *J. Catal.*, 2018, **368**, 389–410.
7 A. Corma, V. Fornes, S. B. Pergher, T. L. M. Maesen and J. G. Buglass, *Nature*, 1998, **396**, 353–356.

8 N. Y. Chen, T. F. Dengnan and C. Morris Smith, *Molecular Transport and Reaction in Zeolites: Design and Application of Shape Selective Catalysts*, John Wiley & Sons, 1994.
9 R. Gounder and E. Iglesia, *Chem. Commun.*, 2013, **49**, 3491–3509.
10 A. Corma, M. Iglesias and F. Sánchez, *Catal. Lett.*, 1996, **39**, 153–156.
11 R. Gounder and M. E. Davis, *J. Catal.*, 2013, **308**, 176–188.
12 J. C. Vega-Vila, J. W. Harris and R. Gounder, *J. Catal.*, 2016, **344**, 108–120.
13 H. Y. Luo, J. D. Lewis and Y. Roman-Leshkov, *Annu. Rev. Chem. Biomol. Eng.*, 2016, **7**, 663–692.
14 Y. Wang, J. D. Lewis and Y. Román-Leshkov, *ACS Catal.*, 2016, 2739–2744, DOI: 10.1021/acscatal.6b00561.
15 P. Müller, S. P. Burt, A. M. Love, W. P. McDermott, P. Wolf and I. Hermans, *ACS Catal.*, 2016, **6**, 6823–6832.
16 J. S. Bates and R. Gounder, *J. Catal.*, 2018, **365**, 213–226.
17 J. S. Bates, B. C. Bukowski, J. W. Harris, J. Greeley and R. Gounder, *ACS Catal.*, 2019, **9**, 6146–6168.
18 M. Boronat, A. Corma, M. Renz and P. M. Viruela, *Chem. – Eur. J.*, 2006, **12**, 7067–7077.
19 S. Conrad, P. Wolf, P. Müller, H. Orsted and I. Hermans, *ChemCatChem*, 2017, **9**, 175–182.
20 Z. Zhu, H. Xu, J. Jiang and P. Wu, *J. Phys. Chem. C*, 2016, **120**, 23613–23624.
21 D. T. Bregante, P. Priyadarshini and D. W. Flaherty, *J. Catal.*, 2017, **348**, 75–89.
22 D. T. Bregante and D. W. Flaherty, *J. Am. Chem. Soc.*, 2017, **139**, 6888–6898.
23 D. T. Bregante, N. E. Thornburg, J. M. Notestein and D. W. Flaherty, *ACS Catal.*, 2018, **8**, 2995–3010.
24 D. T. Bregante, A. M. Johnson, A. Y. Patel, E. Z. Ayla, M. J. Cordon, B. C. Bukowski, J. Greeley, R. Gounder and D. W. Flaherty, *J. Am. Chem. Soc.*, 2019, **141**, 7302–7319.
25 A. Corma, L. Nemeth, M. Renz and S. Valencia, *Nature*, 2001, **412**, 423–425.
26 N. M. Wilson, D. T. Bregante, P. Priyadarshini and D. W. Flaherty, *Catalysis*, 2017, **29**, 122–212.
27 M. Moliner, Y. Roman-Leshkov and M. E. Davis, *Proc. Natl. Acad. Sci. U. S. A.*, 2010, **107**, 6164–6168.
28 T. Blasco, M. A. Camblor, A. Corma, P. Esteve, J. M. Guil, A. Martinez, J. A. Perdigon-Melon and S. Valencia, *J. Phys. Chem. B*, 1998, **102**, 75–88.
29 N. Morlanés and J. M. Notestein, *J. Catal.*, 2010, **275**, 191–201.
30 J. M. Notestein, E. Solovyov, L. R. Andrini, F. G. Requejo, A. Katz and E. Iglesia, *J. Am. Chem. Soc.*, 2007, **129**, 15585–15595.
31 D. T. Bregante and D. W. Flaherty, *ACS Catal.*, 2019, **9**, 10951–10962.
32 I. Takahara, M. Saito, M. Inaba and K. Murata, *Catal. Lett.*, 2005, **105**, 249–252.
33 J. N. Kondo, K. Ito, E. Yoda, F. Wakabayashi and K. Domen, *J. Phys. Chem. B*, 2005, **109**, 10969–10972.
34 S. Sultana Poly, S. M. A. Hakim Siddiki, A. S. Touchy, S. Yasumura, T. Toyao, Z. Maeno and K.-I. Shimizu, *J. Catal.*, 2018, **368**, 145–154.
35 W. Dai, C. Wang, B. Tang, G. Wu, N. Guan, Z. Xie, M. Hunger and L. Li, *ACS Catal.*, 2016, **6**, 2955–2964.
36 E. V. Anslyn and D. A. Dougherty, *Modern Physical Organic Chemistry*, University Science, 2005.
37 P. Wu and T. Tatsumi, *Chem. Commun.*, 2002, 1026–1027.
38 B. Tang, W. Dai, G. Wu, N. Guan, L. Li and M. Hunger, *ACS Catal.*, 2014, **4**, 2801–2810.
39 B. Tang, W. Dai, X. Sun, N. Guan, L. Li and M. Hunger, *Green Chem.*, 2014, **16**, 2281–2291.
40 S. Kulprathipanja, *Zeolites in Industrial Separation and Catalysis*, Wiley-VCH, 2010.
41 Y. Kunitake, T. Takata, Y. Yamasaki, N. Yamanaka, N. Tsunoji, Y. Takamitsu, M. Sadakane and T. Sano, *Microporous Mesoporous Mater.*, 2015, **215**, 58–66.
42 T. Takata, N. Tsunoji, Y. Takamitsu, M. Sadakane and T. Sano, *Microporous Mesoporous Mater.*, 2017, **246**, 89–101.
43 G. M. Lari, P. Y. Dapsens, D. Scholz, S. Mitchell, C. Mondelli and J. Pérez-Ramírez, *Green Chem.*, 2016, **18**, 1249–1260.
44 M. Trejda, A. Wojtaszek, A. Floch, R. Wojcieszak, E. M. Gaigneaux and M. Ziolek, *Catal. Today*, 2010, **158**, 170–177.
45 Y. Kuwahara, J. Aoyama, K. Miyakubo, T. Eguchi, T. Kamegawa, K. Mori and H. Yamashita, *J. Catal.*, 2012, **285**, 223–234.
46 Verified Syntheses of Zeolitic Materials, http://www.iza-online.org/synthesis/default.htm.
47 N. M. Wilson, J. Shroder, P. Priyadarshini, D. T. Bregante, S. Kunz and D. W. Flaherty, *J. Catal.*, 2018, **368**, 261–274.
48 M. Thommes, K. Kaneko, A. V. Neimark, J. P. Olivier, F. Rodriguez-Reinoso, J. Rouquerol and K. S. W. Sing, *Pure Appl. Chem.*, 2015, **87**, 1051–1069.
49 E. L. First, C. E. Gounaris, J. Wei and C. A. Floudas, *Phys. Chem. Chem. Phys.*, 2011, **13**, 17339–17358.
50 N. E. Thornburg, A. B. Thompson and J. M. Notestein, *ACS Catal.*, 2015, **5**, 5077–5088.
51 D. T. Bregante, A. Y. Patel, A. M. Johnson and D. W. Flaherty, *J. Catal.*, 2018, **364**, 415–425.
52 R. P. Vitiello, J. M. Macak, A. Ghicov, H. Tsuchiya, L. F. P. Dick and P. Schmuki, *Electrochem. Commun.*, 2006, **8**, 544–548.
53 Y. Zhao, X. Zhou, L. Ye and S. C. E. Tsang, *Nano Rev.*, 2012, **3**, 17631.
54 W. Chun, A. Ishikawa, H. Fujisawa, T. Takata, J. N. Kondo, M. Hara, M. Kawai, Y. Matsumoto and K. Domen, *J. Phys. Chem. B*, 2003, **107**, 1798–1803.
55 K. Reimann and N. Steube, *Solid State Commun.*, 1998, **105**, 649–652.
56 W. R. Gunther, V. K. Michaelis, R. G. Griffin and Y. Román-Leshkov, *J. Phys. Chem. C*, 2016, **120**, 28533–28544.
57 C. Li, G. Xiong, Q. Xin, J. Liu, P. Ying, Z. Feng, J. Li, W. Yang, Y. Wang, G. Wang, X. Liu, M. Lin, X. Wang and E. Min, *Angew. Chem., Int. Ed.*, 1999, **38**, 2220–2222.
58 A. M. Prakash and L. Kevan, *J. Am. Chem. Soc.*, 1998, **120**, 13148–13155.
59 Y. S. Ko and W. S. Ahn, *Microporous Mesoporous Mater.*, 1999, **30**, 283–291.
60 L. L. Noc, C. C. Moulin, S. Solomykina, D. Trong On, C. Lortie, S. Lessard and L. Bonneviot, *Stud. Surf. Sci. Catal.*, 1995, **97**, 19–25.

 

61 M. T. Melchor, D. E. W. Vaughan and C. F. Pictroski, *J. Phys. Chem.*, 1995, **99**, 6128–6144.
62 S. Prodinger, M. A. Derewinski, A. Vjunov, S. D. Burton, I. Arslan and J. A. Lercher, *J. Am. Chem. Soc.*, 2016, **138**, 4408–4415.
63 S. Prodinger, H. Shi, S. Eckstein, J. Z. Hu, M. V. Olarte, D. M. Camaioni, M. A. Derewinski and J. A. Lercher, *Chem. Mater.*, 2017, **29**, 7255–7262.
64 K. Hadjiivanov, E. Ivanova, R. Kefirov, J. Janas, A. Plesniar, S. Dzwigaj and M. Che, *Microporous Mesoporous Mater.*, 2010, **131**, 1–12.
65 J. Szanyi, J. H. Kwak and C. H. F. Peden, *J. Phys. Chem. B*, 2004, **108**, 3746–3753.
66 R. Gounder, A. J. Jones, R. T. Carr and E. Iglesia, *J. Catal.*, 2012, **286**, 214–223.
67 P. Wolf, C. Hammond, S. Conrad and I. Hermans, *Dalton Trans.*, 2014, **43**, 4514–4519.
68 T. Barzetti, E. Selli, D. Moscotti and L. Forni, *J. Chem. Soc., Faraday Trans.*, 1996, **92**, 1401–1407.
69 J. N. Kondo, R. Nishitani, E. Yoda, T. Yokoi, T. Tatsumi and K. Domen, *Phys. Chem. Chem. Phys.*, 2010, **12**, 11576–11586.
70 F. Tielens, T. Shishido and S. Dzwigaj, *J. Phys. Chem. C*, 2010, **114**, 3140–3147.
71 S. Dzwigaj, Y. Millot and M. Che, *Catal. Lett.*, 2010, **135**, 169–174.
72 B. Tang, W. Dai, X. Sun, G. Wu, N. Guan, M. Hunger and L. Li, *Green Chem.*, 2015, **17**, 1744–1755.
73 R. J. Madon and M. Boudart, *Ind. Eng. Chem. Fundam.*, 1982, **21**, 438–447.
74 J. W. Harris, J. Arvay, G. Mitchell, W. N. Delgass and F. H. Ribeiro, *J. Catal.*, 2018, **365**, 105–114.
75 I. Chorkendorff and J. W. H. Niemantsverdriet, *Concepts of Modern Catalysis and Kinetics*, Wiley-VCH Verlag Gmbh & Co., Weinheim, 2nd edn, 2007.